

# Multiaxial Vibration Fatigue – A Theoretical and Experimental Comparison

Matjaž Mršnik, Janko Slavič, Miha Boltežar  
Faculty of Mechanical Engineering, University of Ljubljana, Slovenia

June 7, 2016

**Cite as:**

**Matjaž Mršnik, Janko Slavič and Miha Boltežar**  
**Multiaxial Vibration Fatigue – A Theoretical and Experimental Comparison.**  
**Mechanical Systems and Signal Processing, Vol. 76–77, p. 409–423, 2016.**  
**DOI: 10.1016/j.ymsp.2016.02.012**

**Abstract**

Random vibration excitation is a common cause of failure, especially when the vibration is in the range of natural frequencies, where the stress response is greatly amplified. A vibration-fatigue analysis can be performed for a high-cycle regime consisting of a structural dynamics analysis, a response calculation and a fatigue analysis. The material parameters (S-N curve) are defined for a constant-amplitude, cyclical, uniaxial stress state. However, in real structures the stress state due to the structural dynamics is rarely uniaxial and direct application of the S-N curve is difficult. The stress tensor is reduced to a more manageable representation using a multiaxial criterion. A multitude of such criteria are available in the literature. In this study, a group of multiaxial criteria are compared theoretically and experimentally, *i.e.*, maximum normal stress, maximum shear stress, maximum normal-and-shear stress, C-S criterion, Projection-by-Projection and the Preumont and Piéfort criterion. A special specimen is used in the experiments that experiences a rich structural response which causes fatigue failure. The experimental comparison of the crack location and the time-to-failure gives comparable results for the tested multiaxial criteria with a reliable time-to-failure estimation. From the research it follows that the crack-location estimation is not accurate enough for either of the compared criteria. The study proves the applicability of the vibration-fatigue analysis procedure (*i.e.*, from excitation, structural dynamics, multiaxial criteria to spectral moment methods) on real vibrating structures with rich structural dynamics.

## Nomenclature

$\mathbf{a}$	vector of coefficient for a critical-plane multiaxial criterion
$C$	S-N curve parameter
$\mathbf{C}$	covariance matrix
$d(\cdot)$	damage intensity of a random uniaxial process
$d_{\text{TB}}$	damage density according to Tovo-Benasciutti
$\mathbf{D}$	damping matrix
$E[\cdot]$	expected value
$\mathbf{H}(\omega)$	transfer matrix
$H_{jk}$	element of the transfer matrix
$\mathbf{I}$	identity matrix
$J_{\text{ref}}$	coefficient of the reference S-N curve
$J_{\text{axi}}$	coefficient of the axial S-N curve
$J_{\text{tor}}$	coefficient of the torsional S-N curve
$k$	S-N curve parameter
$K$	material fatigue coefficient
$\mathbf{K}$	stiffness matrix
$k_{\text{ref}}$	slope of the reference S-N curve
$k_{\text{axi}}$	slope of the axial S-N curve
$k_{\text{tor}}$	slope of the torsional S-N curve
$l_i, m_i, n_i$	directional cosine of the principal stress axes
$m_i$	$i$ -th spectral moment
$\mathbf{M}$	mass matrix
$\mathbf{Q}$	von Mises coefficient matrix
$S(\omega)$	power spectral density (PSD)
$\mathbf{S}_s(\omega)$	stress cross-spectral density matrix
$\mathbf{S}_{\mathbf{x}}(\omega)$	displacements cross-spectral density matrix
$S_{xx,xx}(\omega)$	auto-spectral density of a tensor component
$S_{\text{eq}}(\omega)$	equivalent uniaxial auto-spectral density
$s_c^2$	equivalent von Mises stress according to Preumont and Piéfort
$s_x$	component of the stress tensor in the time domain
$\mathbf{s}$	vector of six independent stress-tensor components
$s_{\text{inv}}$	stress invariant in 5-dimensional space
$\mathbf{s}'$	stress-tensor deviator components vector
$\mathbf{S}_{\text{inv}}(\omega)$	stress invariant cross-spectral density matrix
$s_h$	hydrostatic stress
$\mathbf{S}_U(\omega)$	transformed stress-invariant cross-correlation matrix
$\mathbf{U}$	covariance matrix eigenvectors
$\mathbf{x}(t)$	time-dependent displacements
$\alpha_i$	spectral width parameter
$\eta_{\text{TB}}$	coefficient of the Tovo-Benasciutti method
$\eta_r$	damping loss factor (hysteretic)
$\nu_0^+$	expected positive zero-crossing frequency
$\nu$	expected peak frequency
$\rho_{\text{rho}}$	multiaxial coefficient
$\sigma^2$	variance
$\sigma_{\text{af}}$	fully-reversed bending-fatigue limit
$\tau_{\text{af}}$	fully-reversed torsion-fatigue limit
$\phi_{jr}$	element of the modal mass-normalized matrix
$\omega$	angular frequency
$\Omega_i(\omega)$	uncorrelated uniaxial process according to the PbP method

# 1 Introduction

Broadband random excitation is a source of repeating load on a structure, originating from environmental sources such as a rough road and sea currents, but also machinery such as combustion and propulsion engines [1]. The stress response in a material is amplified at the system's resonances [2], causing a deterioration also known as vibration fatigue [3, 4, 5, 1]. The complete vibration-fatigue procedure is performed in the frequency domain, which carries significant benefits, most notably, fast calculation times and an efficient yet rigorous assessment of random processes [6, 7]. It consists of a structural dynamics analysis, random response calculation and fatigue analysis. Stress-based (high-cycle) fatigue-analysis procedures are based on the distribution of the amplitudes of damaging stress cycles in the time [8, 9, 10] or frequency domain [11, 12]; however, the cycle counting and damage summation on the six independent stress-tensor components is not a straightforward task. A plethora of multiaxial criteria, in the time [13, 14, 15, 16] and frequency domains [3, 17, 18, 19], are available in the literature, enabling the use of methods devised for a uniaxial stress state on more general, multiaxial, complex stress states.

Comparison studies focus on either the time- [20, 21, 22, 23, 24] or frequency-domain formulations [25, 3, 26]. Most of the experimental research is performed on specimens loaded in a quasi-static regime (without considering the effects of the structural dynamics), showing good agreement with the experimental results [27, 28]. However, such studies are rare for a vibrating structure, where the stress state is a consequence of the dynamic response [29]. Furthermore, few studies are available that exploit the broadband random excitation and structural dynamics to induce failure [30, 31, 32, 33]. There is still a lot of uncertainty as to what level of accuracy for the crack location and the time-to-failure estimation can be achieved.

The focus of this study is therefore on a theoretical and experimental comparison of multiaxial criteria for a structural dynamics analysis in the frequency domain. The following criteria are compared side-by-side: maximum normal stress [3], maximum shear stress [3], maximum normal-and-shear stress [3], C-S criterion [34], Projection-by-Projection [19] and the Preumont and Piéfort criterion [35, 28].

In this research, an experimental setup is presented for a fatigue combination resulting from two modal-shape responses. A special Y-sample is excited with two uncorrelated random vibration sources until failure. Two mode shapes are excited, and if one or the other is excited more, the time-to-failure and the failure location are effected. This approach simulates very closely the real-world scenario of a complex structure, vibrating due to broadband random excitation. Furthermore, a FEM numerical approach is presented for the estimation of the crack location and the time-to-failure.

This research is organized as follows. The basic theory of random processes, structural dynamics and fatigue analysis is presented in Section 2. The compared multiaxial criteria are presented in Section 3. Next, the experimental setup and procedure are described in Section 4, followed by the numerical model of the structure and the vibration-fatigue analysis in Section 5. Finally, the results and conclusions are presented in Sections 6 and 7.

## 2 Stress-based fatigue in the frequency domain

Vibration fatigue requires a systematic approach to dealing with random stress tensors in the frequency domain. The basic theory is described in the following sections. Detailed descriptions can be found in Bendat and Piersol [36], Newland [37], Maia et al. [2], Niesłony and Macha [3] and Socie [4].

### 2.1 Uni-axial random process

Normal-distributed random processes are theoretically well defined and offer a convenient way of modeling random excitation and response. The process can be described by the power spectral density (PSD)  $S(\omega)$ . It is further characterized by the moments  $m_i$ :

$$m_i = \int_{-\infty}^{\infty} \omega^i S(\omega) d\omega \quad (1)$$

which convey information about the properties that the process exhibits in the time domain, *e.g.*, variance  $\sigma^2$ , expected positive crossings rate  $\nu_0^+$ , expected peak rate  $\nu$  and the spectral width parameter  $\alpha_i$  [36, 37]:

$$\nu_0^+ = \frac{1}{2\pi} \sqrt{\frac{m_2}{m_0}} \quad \nu = \frac{1}{2\pi} \sqrt{\frac{m_4}{m_2}} \quad \alpha_i = \frac{m_i}{\sqrt{m_0 m_{2i}}} \quad (2)$$

The cycle-amplitude probability density can be estimated based on the spectral moments, using one of the frequency-domain counting methods [12], *e.g.*, the narrowband method [38], Dirlik [39] or Tovo-Benasciutti [11], of which the Tovo-Benasciutti damage intensity  $d_{TB}$  is given here:

$$d_{TB} = [\eta_{TB} + (1 - \eta_{TB}) \alpha_2^{k-1}] \alpha_2 d_{NB} \quad (3)$$

where  $k$  is the material fatigue parameter,  $d_{NB}$  defines the narrowband damage intensity and  $\eta_{TB}$  was chosen by the authors [11] and is based on numerical simulations:

$$d_{NB} = \nu_0^2 C^{-1} (\sqrt{2m_0})^k \Gamma\left(1 + \frac{k}{2}\right) \quad (4)$$

$$\eta_{TB} = \frac{(\alpha_1 - \alpha_2) [1.112 (1 + \alpha_1 \alpha_2 - (\alpha_1 + \alpha_2)) e^{2.11 \alpha_2} + (\alpha_1 - \alpha_2)]}{(\alpha_2 - 1)^2} \quad (5)$$

the S-N curve is used for high-cycle stress-based fatigue, conveying specific material properties in an analogous way to the time-domain analysis procedure. They are given with the constants  $C$  and  $k$ , thus defining the SN parabola, which defines the relationship between the number of cycles-to-failure  $N$  for a constant cycle amplitude  $s$  [11]:

$$C = s^k N \quad (6)$$

## 2.2 Structural dynamics analysis

A description of the stress state in a material is needed before a fatigue analysis can be performed. One possible way to deduce the stress responses, based on a modal model, is described in the following. The modal model of a multi-degree-of-freedom (MDOF) system is obtained from a frequency analysis of the FEM model, for which the equilibrium equations are defined [2]:

$$\mathbf{M} \ddot{\mathbf{x}}(t) + \mathbf{K} \mathbf{x}(t) + \mathbf{D} \dot{\mathbf{x}}(t) = \mathbf{f}(t) \quad (7)$$

comprising the mass matrix  $\mathbf{M}$ , the damping matrix  $\mathbf{D}$ , the stiffness matrix  $\mathbf{K}$ , the force  $\mathbf{f}(t)$  and the displacements  $\mathbf{x}(t)$ . The solution of the eigenvalue problem gives the eigenfrequencies and eigenmodes, characterizing the dynamic properties of the MDOF structure. Modes are decoupled and the modal superposition approach is used to further deduce the response model, which conveniently provides the relationship between the excitation  $\mathbf{F}$  and the response  $\mathbf{X}$ :

$$\mathbf{X} = \mathbf{H}(\omega) \mathbf{F} \quad (8)$$

where the  $jk$ -th element of the receptance matrix  $\mathbf{H}(\omega)$  is calculated using an assumption of the hysteretic damping:

$$H_{jk}(\omega) = \sum_{r=1}^N \frac{\phi_{jr} \phi_{kr}}{\omega_r^2 - \omega^2 + i \eta_r \omega_r^2} \quad (9)$$

where  $\omega_r^2$  is the  $r$ -th natural frequency,  $\eta_r$  is the modal damping loss factor for the  $r$ -th natural frequency and  $\phi_{jr}$  is the  $jr$ -th element of the mass-normalised modal matrix  $\boldsymbol{\phi}$  [2]. The resulting receptance matrix offers the possibility of a fast response calculation when the structure is excited by a known force. It also makes it straightforward to update the numeric model with experimentally obtained modal data, *e.g.* substitute experimental modal damping factors into the numerical model.

However, in applications, it is frequently the kinematic excitation that is given. Such is the case for the base motion excitation, which is commonplace in accelerated vibration tests using an electrodynamic shaker. Because the forces in the supports are unknown, the above approach from (8) cannot be used directly. A solution is offered by a structural modification approach, such as the SMURF (structural modification using response functions) method, which will be used in the course of this paper when necessary. It is an impedance-based method for deriving the dynamics of a constrained structure based on an unconstrained model. By splitting the model into constrained and unconstrained parts and performing some clever manipulations of equilibrium equations, the kinematic base-excitation response can be deduced [40].

The transfer-function matrices  $\mathbf{H}_{aa}$  relate the kinematic random excitation  $\mathbf{S}_{\ddot{\mathbf{x}}}(\omega)$  to the acceleration responses for the purposes of model updating. The transfer-function matrices  $\mathbf{H}_{as}$  relate the excitation to the stress responses [41] for the purposes of the fatigue analysis:

$$\mathbf{S}_s(\omega) = \mathbf{H}_{as}^*(\omega) \mathbf{H}_{as}(\omega) \mathbf{S}_{\ddot{\mathbf{x}}}(\omega) \quad (10)$$

Analogously, the  $\mathbf{H}_{fa}$  and  $\mathbf{H}_{fs}$  are needed for the force-response calculation, while the indices  $\mathbf{fa}$  and  $\mathbf{fs}$  convey the force-to-acceleration and the force-to-stress FRFs, respectively. The stresses  $\mathbf{S}_s(\omega)$  are described in the frequency domain by the auto-spectral and cross-spectral densities of the six independent stress-tensor components in the form of a  $6 \times 6$  matrix:

$$\mathbf{S}_s(\omega) = \begin{bmatrix} S_{xx,xx}(\omega) & \dots & S_{xx,yz}(\omega) \\ \vdots & \ddots & \vdots \\ S_{yz,xx}(\omega) & \dots & S_{yz,yz}(\omega) \end{bmatrix} \quad (11)$$

### 3 Multi-axial criteria

Multi-axial criteria approach the reduction of the stress components from Eq. (11) in different ways, but can usually be placed in one of two groups: stress-invariant methods and critical-plane methods. The invariant-calculation methods produce a result for the material point, regardless of the orientation of the critical plane, while critical-plane methods produce different results on different planes at this same material point. The experimental data shows [21, 20, 42] that the critical-plane methods are better suited to proportional loads (principal axes are fixed), while the stress-invariant-based methods are better suited to non-proportional loads (the principal axes rotate with time).

In the following sections a group of selected multi-axial criteria formulated for the frequency domain are presented. The criteria that were experimentally compared are as follows: maximum normal stress [3], maximum shear stress [3], maximum normal and shear stress [3], Preumont and Piéfort [28], C-S criterion [34] and the Projection-by-Projection approach [19].

### 3.1 Criteria of the maximum stress on a critical plane

This group of criteria determines the equivalent stress  $S_{\text{eq}}(\omega)$  from the combination of stress components on the critical plane. Three different approaches are presented here, adopted from Niesłony and Macha [3], *i.e.*, the maximum normal stress, the maximum shear stress and the criterion of maximum normal-and-shear stress.

The equivalent stress  $S_{\text{eq}}(\omega)$  is interpreted as a single output of a six-input physical system, the six inputs being defined by a linear combination of the components of the stress matrix  $\mathbf{S}_s(\omega)$  from (11):

$$S_{\text{eq}}(\omega) = \mathbf{a} \mathbf{S}_s(\omega) \mathbf{a}^T \quad (12)$$

Each of the three maximum stress criteria is then defined by Eq. (12) and a vector of the coefficients  $\mathbf{a}$  suiting the respective multiaxial criterion, according to Table 2.

Table 2: Coefficients defining the multiaxial criteria [3].

$\mathbf{a}$	Max. normal	Max. shear	Max. normal and shear
$a_1$	$l_1^2$	$(l_1^2 - l_3^2)$	$\frac{1}{1+K} \left[ l_1^2 - l_3^2 + K (l_1^2 + l_3^2)^2 \right]$
$a_2$	$m_1^2$	$(m_1^2 - m_3^2)$	$\frac{1}{1+K} \left[ m_1^2 - m_3^2 + K (m_1^2 + m_3^2)^2 \right]$
$a_3$	$n_1^2$	$(n_1^2 - n_3^2)$	$\frac{1}{1+K} \left[ n_1^2 - n_3^2 + K (n_1^2 + n_3^2)^2 \right]$
$a_4$	$2l_1 m_1$	$2(l_1 m_1 - l_3 m_3)$	$\frac{1}{1+K} [l_1 m_1 - l_3 m_3 + K (l_1 + l_3) (m_1 + m_3)]$
$a_5$	$2l_1 n_1$	$2(l_1 n_1 - l_3 n_3)$	$\frac{1}{1+K} [l_1 n_1 - l_3 n_3 + K (l_1 + l_3) (n_1 + n_3)]$
$a_6$	$2m_1 n_1$	$2(m_1 n_1 - m_3 n_3)$	$\frac{1}{1+K} [m_1 n_1 - m_3 n_3 + K (m_1 + m_3) (n_1 + n_3)]$

The  $l_i$ ,  $m_i$  and  $n_i$  are directional cosines of the principal stress axes and  $K$  is the material fatigue coefficient, defined as [42]:

$$K = 2 \frac{\tau_{\text{af}}}{\sigma_{\text{af}}} - 1 \quad (13)$$

$\tau_{\text{af}}$  being the fully reversed torsion-fatigue limit and  $\sigma_{\text{af}}$  being the fully reversed bending-fatigue limit.

#### 3.1.1 Critical plane

The resulting stress function  $S_{\text{eq}}(\omega)$  depends on the angle of the plane for which it is calculated. The angle is usually determined in one of two ways [3]. The first approach suggests calculating the damage for a number of different planes, spaced out equally, and then choosing the one that gives the maximum damage. The second, computationally less intensive, approach used in this study assumes that the critical plane coincides with the plane of maximum variance for the chosen criterion. This speeds up the calculation as the inputs are no longer functions of the frequency, but just scalar values of the (co-)variance ( $\sigma_{xx,xx}^2$ ,  $\sigma_{xx,yy}^2$  ...). The covariance matrix  $\mathbf{C}$  is calculated for this purpose:

$$\mathbf{C} = \begin{bmatrix} \sigma_{xx,xx}^2 & \cdots & \sigma_{xx,yz}^2 \\ \vdots & \ddots & \vdots \\ \sigma_{yz,xx}^2 & \cdots & \sigma_{yz,yz}^2 \end{bmatrix} \quad (14)$$

Based on  $\mathbf{C}$  the plane is searched, giving the maximum value of the variance  $\sigma_{s_{\text{eq}}}^2 = \text{Var}[S_{\text{eq}}]$  for the multiaxial criterion. This is done in an analogous way to the equivalent stress calculation based on Eq. (12).

$$\sigma_{s_{\text{eq}}}^2 = \mathbf{a} \mathbf{C} \mathbf{a}^T \quad (15)$$

While the described approach to a critical-plane search could be used generally, the maximum normal-and-shear stress criterion is treated in a different manner in the course of this study. The critical plane is defined as the plane with the maximum variance of shear stress rather than the plane with the maximum variance of the criterion itself, in accordance with Matake [14].

### 3.2 Preumont and Piéfort criterion

In 1994 Preumont and Piéfort [35] proposed a frequency-domain method to estimate high-cycle fatigue damage based on the definition of the well-known von Mises stress  $s_c$ , defined in the time domain as

$$s_c^2 = s_x^2 + s_y^2 + s_z^2 - s_x s_y - s_x s_z - s_y s_z + 3 (s_{xy}^2 + s_{yz}^2 + s_{xz}^2) \quad (16)$$

If  $\mathbf{s}$  is written in vector form as  $\mathbf{s} = (s_x, s_y, s_z, s_{xy}, s_{xz}, s_{yz})$  Eq. (16) can be reformulated and the expected value of the von Mises stress expressed as:

$$E [s_c^2] = \mathbf{s}^T \mathbf{Q} \mathbf{s} = \text{Trace} \{ \mathbf{Q} E [\mathbf{s} \mathbf{s}^T] \} \quad (17)$$

where  $\mathbf{Q}$  is a coefficient matrix

$$\mathbf{Q} = \begin{bmatrix} 1 & -1/2 & -1/2 & 0 & 0 & 0 \\ -1/2 & 1 & -1/2 & 0 & 0 & 0 \\ -1/2 & -1/2 & 1 & 0 & 0 & 0 \\ 0 & 0 & 0 & 3 & 0 & 0 \\ 0 & 0 & 0 & 0 & 3 & 0 \\ 0 & 0 & 0 & 0 & 0 & 3 \end{bmatrix} \quad (18)$$

The expected value of the product  $E [\mathbf{s} \mathbf{s}^T]$  is actually the expected value of the matrix  $\mathbf{S}_s(\omega)$  from Eq. (11) and is straightforward to calculate, leading to

$$E [s_c^2] = \int_0^\infty \text{Trace} \{ \mathbf{Q} \mathbf{S}(\omega) \} d\omega \quad (19)$$

What Eq. (19) conveys is that the expected value or the mean-square of the von Mises stress is equal for the time-domain and for the frequency-domain formulation. Based on this equality the formulation of a multiaxial criterion is given in the form of [17]:

$$S_c(\omega) = \text{Trace} \{ \mathbf{Q} \mathbf{S}(\omega) \} \quad (20)$$

Benasciutti [43] and Bonte et al. [44] pointed out problems concerning the mathematical rigorosity and physical correctness of this method. However, due to the simplicity of the approach, this is one of the frequently used frequency-domain methods for the equivalent-stress calculation. In fact, a formulation is suggested by Bonte et al. [44] that takes into account the phase between the stress-tensor components. Surprisingly, the effect of the phase-offset reduces the damage of the von Mises method, in contrast to the experimental results, as noted by Niesłony [27].

### 3.3 Carpinteri-Spagnoli criterion

Carpinteri et al. proposed a rather elaborate time-domain, multiaxial criterion in 2001 [45]. The central point of this criterion is to determine the orientation of the critical plane by averaging the principal stress directions, prior to the critical-plane criterion's application. A frequency-domain formulation was proposed in 2014 by Carpinteri et al. in [34]. Once the critical-plane orientation is determined, the equivalent stress is calculated as follows

$$S_{eq}(\omega) = S_{zz}(\omega) + \left( \frac{\sigma_{fr}}{\tau_{fr}} \right) S_{yz}(\omega) \quad (21)$$

where  $\sigma_{fr}$  is the fully reversed bending-fatigue limit and  $\tau_{fr}$  is the fully reversed torsion-fatigue limit.  $S_{zz}(\omega)$  and  $S_{yz}(\omega)$  are defined so that the axes  $x$ ,  $y$  lie on the critical plane, perpendicular to  $z$ . For the derivation of the critical-plane orientation the reader is referred to the original paper [34].

### 3.4 The Projection-by-Projection approach

In 2008 Cristofori et al. [16] proposed a method for deducing the damage based on the second invariant of the stress-tensor deviator. It was later (2011) reformulated for the frequency domain [19]. The stress invariant  $\mathbf{s}_{inv} = (S_1, S_2, S_3, S_4, S_5)$  is defined in the  $E_5$  Euclidean space according to:

$$S_1 = \frac{\sqrt{3}}{2} s'_1 \quad S_2 = \frac{1}{2} (s'_2 - s'_3) \quad S_3 = s'_4 \quad (22)$$

$$S_4 = s'_5 \quad S_5 = s'_6 \quad (23)$$

where  $s' = (s'_1, s'_2, s'_3, s'_4, s'_5, s'_6)$  are the components of the stress-deviator tensor, defined together with the hydrostatic stress  $s_h$ :

$$\mathbf{s} = \mathbf{s}' + \mathbf{I} s_h \quad (24)$$

where  $\mathbf{I}$  is the identity matrix. The essence of the method is the transformation of the cross-spectrum matrix  $\mathbf{S}_{inv} = \mathbf{s}_{inv} \mathbf{s}_{inv}^T$  into the sub-space of eigenvectors of the (stress-invariant) covariance matrix  $\mathbf{C}'$  (see (14)). For this purpose, the eigenvectors  $\mathbf{U}$  of  $\mathbf{C}'$  are obtained, which can be used to transform  $\mathbf{C}'$  into a diagonal matrix  $\mathbf{C}'_0$ :

$$\mathbf{C}'_0 = \mathbf{U}^T \mathbf{C}' \mathbf{U} \quad (25)$$

and are applied to the frequency-domain, stress-state definition  $\mathbf{S}_{inv}(\omega)$ , yielding the transformed matrix of  $\mathbf{S}_U(\omega)$

$$\mathbf{S}_U(\omega) = \mathbf{U} \mathbf{S}_{inv}(\omega) \mathbf{U} \quad (26)$$

A group of five uncorrelated uniaxial processes  $\Omega_i(\omega)$  is thus defined. Each process is treated separately and the damages  $d(\Omega_i)$ , calculated using a chosen spectral moment method are then summed according to a quadratic damage-accumulation rule:

$$d(\Omega) = \left[ \sum_{i=1}^5 (d(\Omega_i))^{\frac{2}{k_{ref}}} \right]^{\frac{k_{ref}}{2}} \quad (27)$$

where  $k_{\text{ref}}$  defines the slope of the reference S-N curve, derived from the axial ( $J_{A,\text{axi}}, k_{\text{axi}}$ ) and torsion ( $J_{A,\text{tor}}, k_{\text{tor}}$ ) S-N curves via the following linear interpolation:

$$\begin{aligned} J_{A,\text{ref}} &= J_{A,\text{tor}} + \rho_{\text{ref}} (J_{A,\text{axi}} - J_{A,\text{tor}}) \\ k_{\text{ref}} &= k_{\text{tor}} + \rho_{\text{ref}} (k_{\text{axi}} - k_{\text{tor}}) \end{aligned} \quad (28)$$

where the reference stress ratio is determined from the load characteristics using:

$$\rho_{\text{ref}} = \sqrt{3} \frac{s_{h,m} + \sqrt{2 m_{0,h}}}{\sqrt{2 \sum_{i=1}^5 m_{0,i}}} \quad (29)$$

## 4 Experiment

A special Y-sample was used in the experiment [32, 46], shown in Fig. 1. It is made from cast aluminum, cut to the specified shape. Weights are affixed to each side, tuning the modal frequencies and the shapes of the specimen, enabling a study of the high-cycle fatigue by exciting the near resonant frequencies. A hole is drilled near the center to facilitate a force-excitation mount, which must successfully resist the relatively large loads. The Y-specimen is attached to the fixture, as shown in Fig. 2.

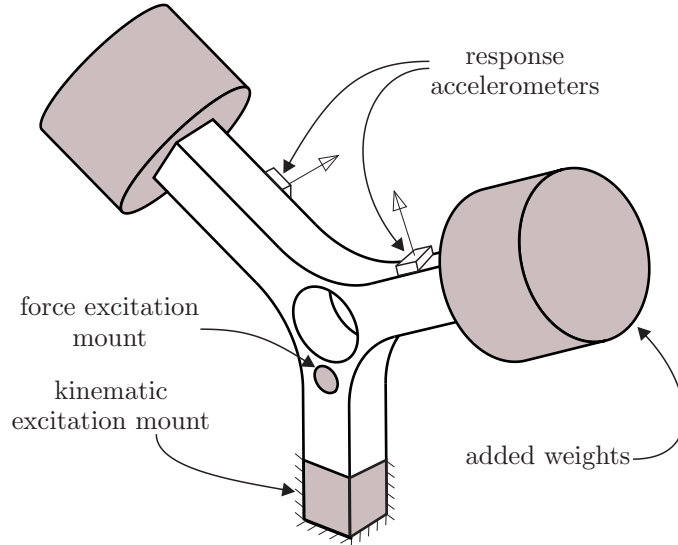


Figure 1: Schematics of the Y-sample.

An accelerometer is mounted on each side of the specimen, as shown in Fig. 1 and 2. At the beginning of the experiment these sensors are used to update the FEM model based on the kinematic response. Throughout the experiment the accelerometers are used to monitor the response in real time in order to measure the mode frequency.

Kinematic excitation is applied in the vertical direction on the fixture. It is controlled in a closed loop with the reference accelerometer. Because of the nature of the controlled kinematic excitation it was possible to ensure a uniform, broadband profile in the frequency range 380–480 Hz. This range covers the natural frequency and its vicinity, even after it drops significantly.

The force excitation is applied perpendicularly near the center of the sample, as shown in Fig. 3. It is controlled with an open loop using a force transducer. The amount of exerted force  $F_{\text{rms}}$  is regulated with a 2-kW power amplifier and the drive-signal voltage profile  $U_{\text{rms}}$  is kept

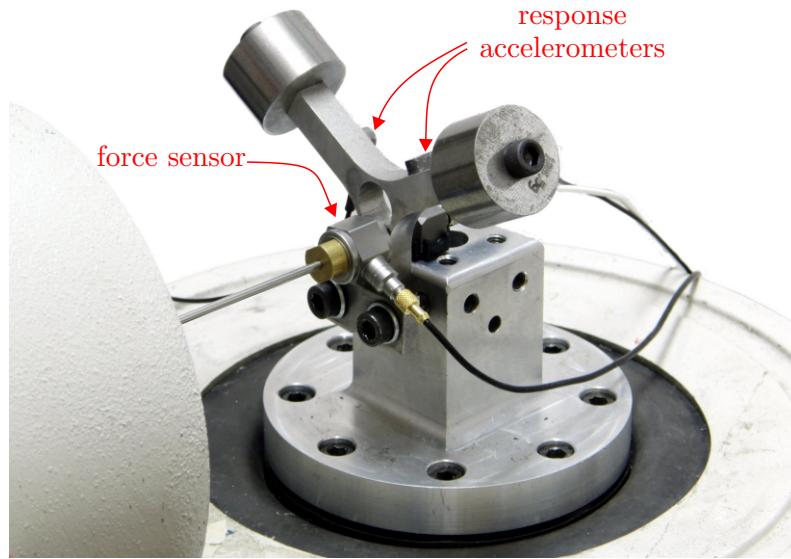


Figure 2: Experimental setup.

constant throughout the experiment. While the drive was a uniform, broadband random signal in the range 290–390 Hz, the force profile measured with the sensor was not uniform as a consequence of the structure-exciter interaction.

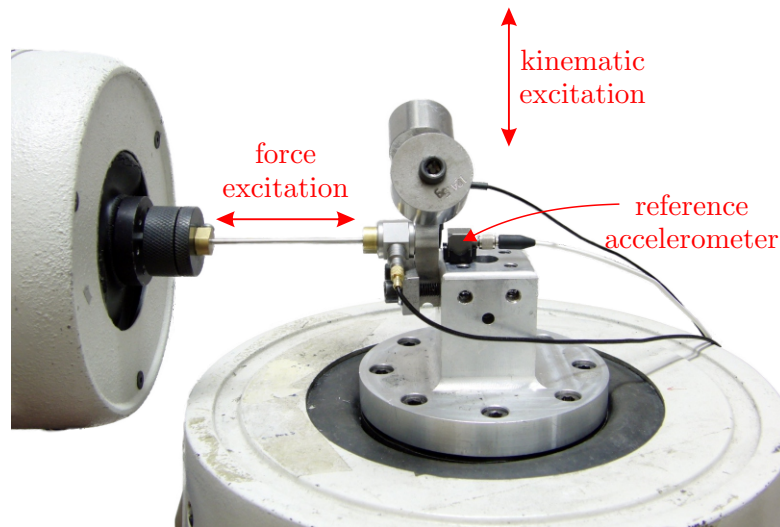


Figure 3: Application of the excitation.

Each load case is defined in advance, as a combination of different kinematic and force broadband random loads. Table 3 shows the loads measured for each load case (specimen). Additionally, the load combinations are visualized in Fig. 4. For each such combination, exactly one specimen is excited until failure, which yields a total of 10 specimens.

#### 4.1 Determining Time-to-failure

Determining the time-to-failure from an experiment is a delicate task. It is unfeasible to load the sample until total failure, because the structural dynamics change much earlier in the process,

Table 3: Force and kinematic load combinations, measured.

load case	$F_{\text{rms}}$ [N]	$a_{\text{rms}}$ [g]
1	2.42	1.25
2	2.51	1.51
3	2.32	1.73
4	3.11	0.86
5	3.36	0.99
6	3.36	1.28
7	3.39	1.49
8	3.94	0.80
9	4.06	1.10
10	3.73	1.27

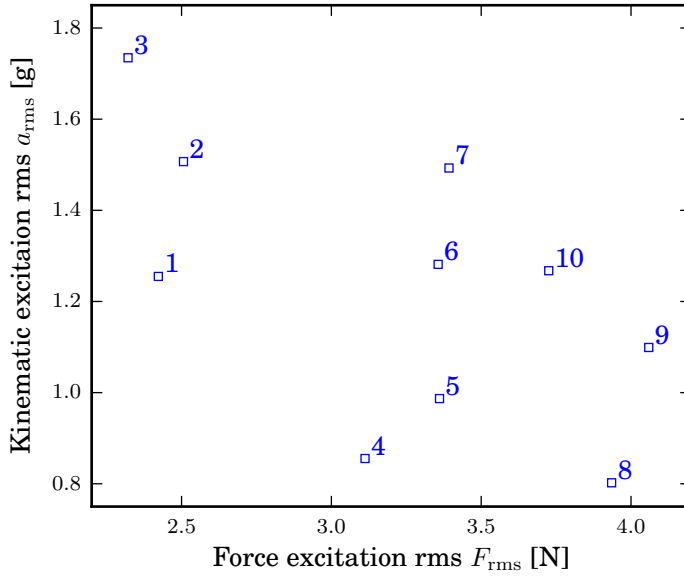


Figure 4: Force and kinematic load combinations, measured.

deviating from the linear numerical model. A damage model is used in its place, which relates the accumulated damage to the natural frequency change, and is straightforward to measure using an accelerometer.

There is a complication due to the fact that while the damage  $d$  is unique for the specimen at hand, the two excited modes experience different changes in natural frequencies  $\Delta\omega_1$  and  $\Delta\omega_2$ , as a consequence of a change in  $d$ .

A frequency-based, damage-detection method (FBDD) by Kim et al. [47] is used, which suggest a proportionality between the damage  $\alpha_j$  inflicted at the location  $j$ , the sensitivity  $F_{ij}$  of a particular mode  $i$  at location  $j$  and a fractional change in the frequency  $Z_i$ :

$$\sum_{j=1}^{\text{NE}} F_{ij} \alpha_j = Z_i \quad (30)$$

where  $Z_i = \Delta\omega_i^2/\omega_{i,0}^2$  and NE is the number of elements. For the purpose of this study, the sensitivities for different elements are assumed to be equal and a fraction of  $Z_i = 5\%$  (of a drop of angular frequency  $\omega_{i,0}$ ) is used to determine the failure, equivalently for both excited modes ( $Z_i = Z_1 = Z_2$ ). Based on the definition of  $Z_i$ , a change of the angular frequency corresponding to a fractional drop in the natural frequency  $\Delta\omega_i$  of 5%, can be derived:

$$\Delta\omega_i = \omega_{i,0} - \sqrt{\omega_{i,0}^2 - 0.05\omega_{i,0}^2} \quad (31)$$

where the  $\omega_{i,0}$  for both modes ( $i = 1, 2$ ) is determined separately for each specimen at the beginning of the experiment.

## 5 Vibration-Fatigue Analysis

A linear numerical model was used to produce time-to-failure estimates. It was prepared with the finite-element method (FEM), and commercial software was used to extract the first eight eigenmodes of the undamped model (up to 3285 Hz). Subsequent calculations were performed using software routines prepared by the authors. First, eigenmodes and experimental modal damping data were used to derive the force response for mode I at 355 Hz and the kinematic base-excitation response for mode II at 472 Hz. The modal-superposition and structural-modification techniques were used to arrive at the responses. The modal shapes, are shown together with the undeformed model in Fig. 5 and 6.

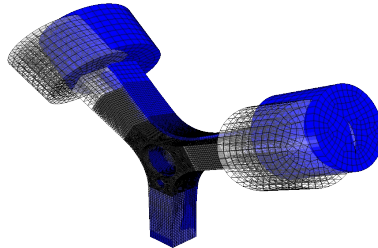


Figure 5: Modal shape I.

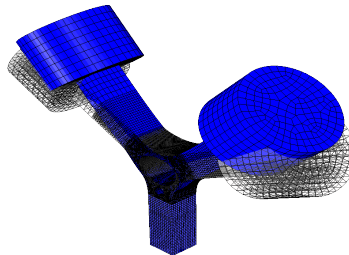


Figure 6: Modal shape II.

The comparison of the calculated and measured FRF is shown in Fig. 7 and 8 for each of the excited modes, for the relevant frequency ranges. The relative error, in comparison with the experiment, is 2.5% for mode I and 0.9% for mode II.

Hysteretic damping was identified on the experimental data using the circle-fit method [2] and the yet to be released open source software OpenModal [?]. The excitation profile measured in the experiment was used to update the numerical model and deduce the stress responses. This procedure was performed for each specimen, thus improving the accuracy of the stress responses, as the damping values can vary slightly between specimens.

The stress responses are calculated for each mode shape separately and summed in the frequency domain, assuming that the excitation sources are uncorrelated:

$$\mathbf{S}_s(\omega) = \mathbf{S}_1(\omega) + \mathbf{S}_2(\omega) \quad (32)$$

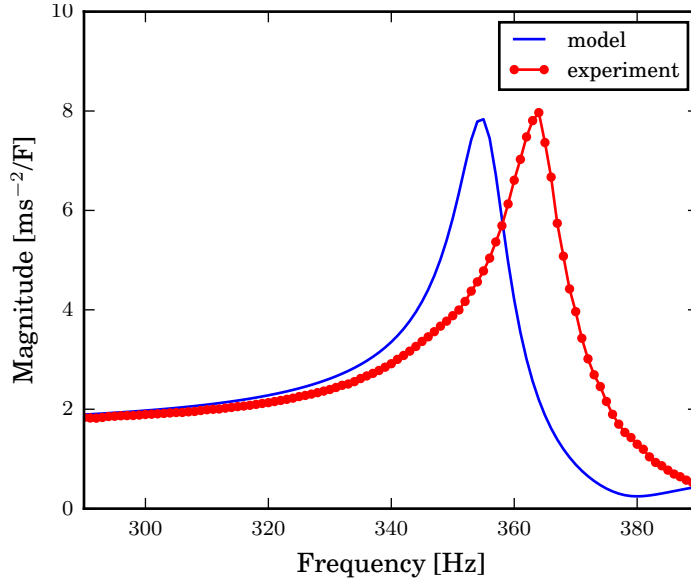


Figure 7: Comparison of calculated and measured frequency-response function of the structure in the frequency range and the direction of the force excitation.

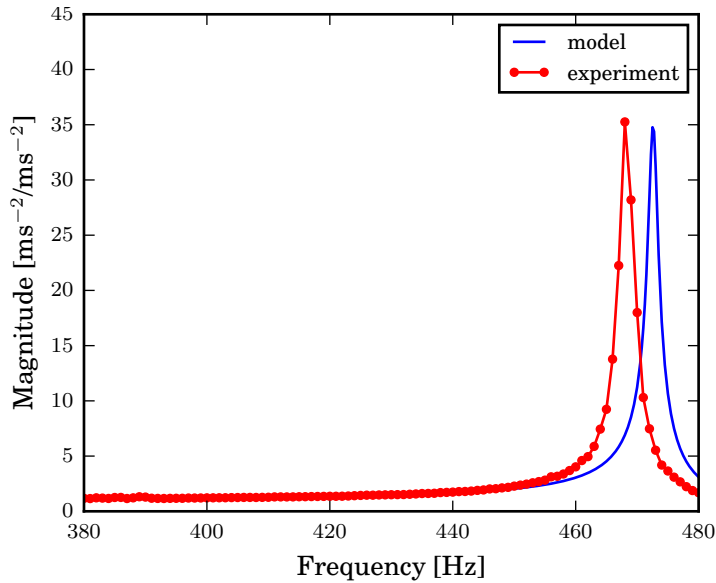


Figure 8: Comparison of calculated and measured frequency-response function of the structure in the frequency range and the direction of the acceleration excitation.

where  $\mathbf{S}_1$  and  $\mathbf{S}_2$  are the responses for each mode and  $\mathbf{S}_s$  is the combined response, which is fed to the multi-axial criterion.

Based on the calculated responses the multi-axial criteria were applied to obtain the final time-to-failure. Using the optimization procedure such material parameters were chosen that minimized the difference with respect to the experimental results. In the first pass, generic material data was used to deduce the critical node. The L-BFGS-B [48] optimization procedure was used next, to produce the optimum material parameters, by minimizing the sum of the square of difference between numerical  $t_{i,num}$  and experimental times to failure  $t_{i,exp}$ .

$$\sum_i (t_{i,\text{exp}} - t_{i,\text{num}})^2 \quad (33)$$

across all samples  $i$ . The optimization was applied for the S-N curve data only, for each multiaxial criterion separately. The C-S approach and the criteria for the maximum normal and shear stress require additional material data, which were unavailable for the particular aluminum alloy (AlSi7Cu3) used in this study. The values of the fully reversed bending limit  $\sigma_{\text{af}} = 161$  and the fully reversed torsion limit  $\tau_{\text{af}} = 97$  were taken from the literature [49] for the aluminum alloy AlCuMg1.

## 6 Results and Comparisons

When analyzing the results it is important to keep in mind that the estimates are the final output of the structural dynamics analysis, spectral moment methods and the experimental measurements, each being a source of error. However, as the procedure chain for calculating the time-to-failure is very similar for each of the criteria, the side-by-side comparison gives a very useful insight into how these criteria perform and at the same time draws conclusions about the accuracy and performance of the complete vibration-fatigue analysis procedure.

### 6.1 Time-to-Failure Comparison

The time-to-failure ranges from 20 min to 135 min, yielding from  $9 \times 10^5$  to  $6 \times 10^6$  of damage cycles, falling well into the domain of high-cycle fatigue. The S-N curve parameters, obtained through the optimization procedure, are given in Table 4. One has to keep in mind, that this material data is closely tied to the Y-specimen and its dynamic properties and can not be directly compared to cyclic test results.

Table 4: S-N curve parameters, that provided the best fit of experimental and numerical results.

Multiaxial criterion	$C$ [MPa $^k$ ]	$k$
Max. shear stress	$4.71 \times 10^{22}$	1.92
Max. normal stress	$5.37 \times 10^{23}$	2.18
Preumont and Piéfort	$4.99 \times 10^{21}$	1.92
Projection-by-Projection	$2.23 \times 10^{18}$	1.71
Carpinteri-Spagnoli	$3.83 \times 10^{18}$	1.51
Max. normal-and-shear s.	$1.11 \times 10^{21}$	1.85

A look at the time-to-failure correlation between the theory and experiment (see Fig. 9, also representative for all the other multiaxial criteria) reveals that the criteria give reasonably accurate results.

Most of the estimates are within  $\pm 200\%$  of the experimental results (dashed line) and only a few deviate by  $\pm 300\%$  or more (dotted line). A side-by-side comparison is provided in Fig. 10, plotting the relative difference  $D$  between the experimental and numerical results:

$$D = \frac{t_{\text{exp}} - t_{\text{num}}}{t_{\text{exp}}} \quad (34)$$

where  $t_{\text{exp}}$  is the experimental time-to-failure and  $t_{\text{num}}$  is the numerical estimate. This comparison confirms that the results of different multiaxial criteria are relatively close. It also reveals that discrepancies between estimates of different criteria are biggest for the force dominant load cases.

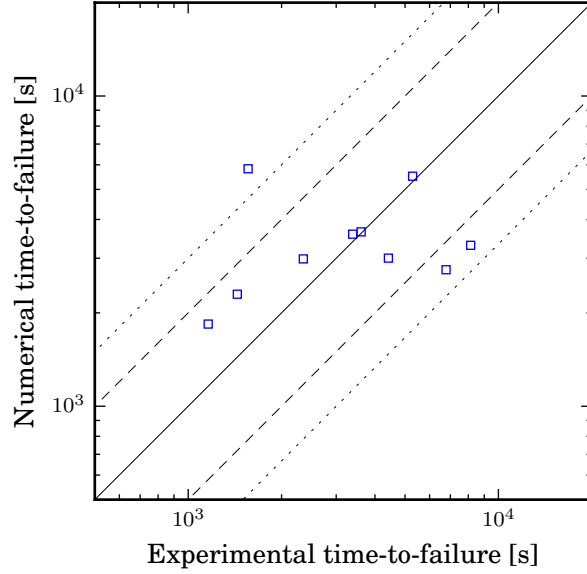


Figure 9: Results for the maximum shear-stress criterion.

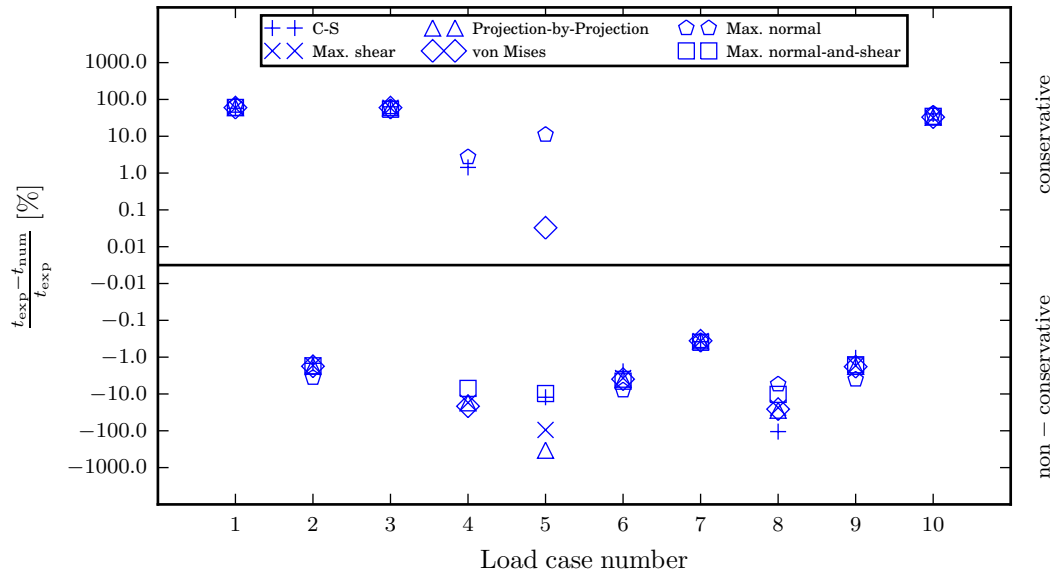


Figure 10: Side-by-side comparison of the time-to-failure estimates for each load case.

## 6.2 Crack-Location Comparison

The side-by-side comparison of the multiaxial criteria reveals that there are only minor variations between the different criteria. This fact is illustrated in Fig. 11, comparing the time-to-failure contours. The minimum of the time-to-failure is not exactly at the same location for each criteria, but they are fairly close, *i.e.*, unable to discern with a simple visual inspection. This trend was observed for all of the compared criteria.

In contrast to the numerical results, the comparison of the experimental results revealed that there is an offset in the crack location which correlates with the load ratio  $\delta = F_{\text{rms}}/a_{\text{rms}}$ . To illustrate this phenomenon, cracked samples are sorted by the value of  $\delta$  in ascending order from left (acceleration dominant load) to right (force dominant load), see Fig. 12. In this way a trend

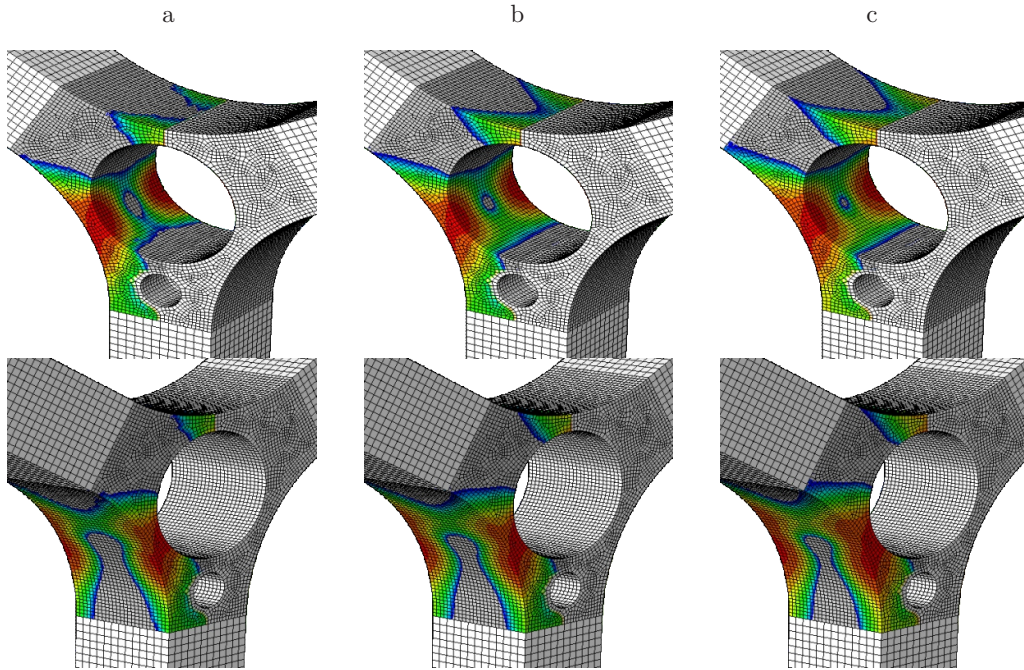


Figure 11: Time-to-failure contour for load case 6, calculated using the Projection-by-Projection approach (a), C-S criterion (b) and Preumont and Piéfort criterion (c).

is evident, although not without scatter: the crack shifts in concert with the  $\delta$  change. Such results demonstrate the combined effect of the interaction of the response stress distributions of two different mode shapes.

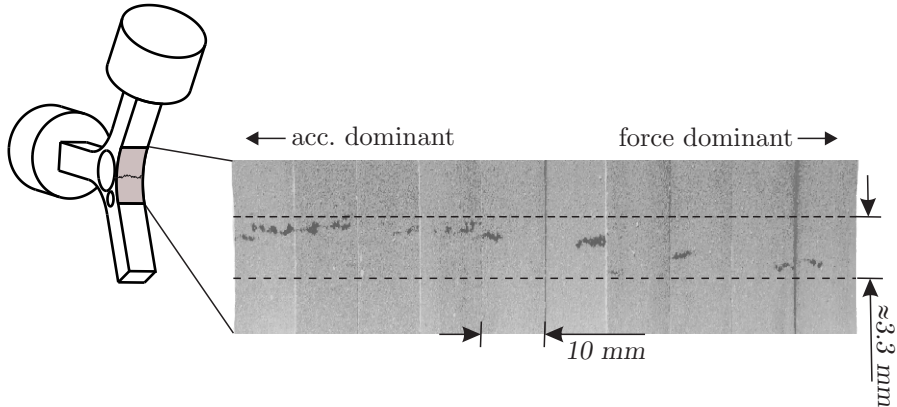


Figure 12: Side-by-side comparison of the crack position in the Y-samples.

A numerical experiment is made at this point, where only one part of the load is applied (force or kinematic). Two critical points  $C_1$  (due to the force load) and  $C_2$  (due to the kinematic load) emerge at different locations, as shown in Fig. 13.

One would then expect, judging from the experimental results, that the critical point for the combined load would lie on a path connecting the two separate critical locations  $C_1$  and  $C_2$ . However, calculations give a somewhat unexpected result. Instead of appearing at intermediate locations, the critical point stays mostly fixed at  $C_1$ , then changes to  $C_2$  for the load case 3 (see Fig. 14). The finite-element size should be sufficiently small at 0.4 mm in the vicinity of the

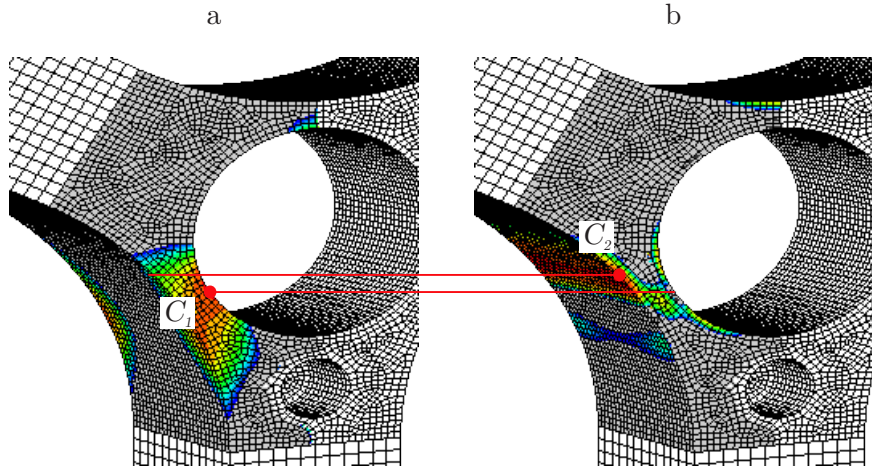


Figure 13: Positions of calculated critical points for the force dominant load  $C_1$  (a) and the acceleration dominant load  $C_2$  (b).

crack, much less than the crack offset, approximately 3 mm. These findings suggest that there are inaccuracies present in the results with regards to the crack location for the case of combined random loads.

It should be noted at this point that the crack position was determined from the grown crack, and that the exact spot of the crack initiation was not identified.

## 7 Conclusions

This paper presents a complete procedure for a vibration-fatigue analysis and its validation. An experiment is performed that simulates the realistic scenario of a vibrating structure with a rich structural response. It is performed with a Y-specimen, brought to failure by a combination of two near-resonance responses of two separate modal shapes. The time-to-failure is determined and compared with the numerical results, using seven different multiaxial criteria, *i.e.*, the maximum normal stress, maximum shear stress, maximum normal-and-shear stress, Preumont and Piéfort, C-S and Projection-by-Projection criterion.

The material load is a consequence of the combination of two different modal stress shapes. In a sense its multiaxiality might have been less pronounced in comparison with the more classical example of the combination of quasi-static bending and torsion. However, the response produced in this study is a very typical structural response and is representative for the case of vibration fatigue, which is caused by the natural response of the structure and not by enforced quasi-static displacements.

There is experimental evidence that the ratio of the severity of two excitation loads, which are applied to the sample at a perpendicular angle by two uncorrelated vibration sources, has an effect on the location of the crack. At the same time this same phenomenon went almost unnoticed in the numerical analyses, raising some concerns about the accuracy of the crack-location estimate, given by the compared multiaxial criteria. Overall, the damage distribution fields, showing the damage intensity (or time-to-failure) on different parts of the specimen, were close for all of the compared multiaxial criteria.

Most time-to-failure estimates fall within the  $\pm 2\times$  band, with only a few outliers. The results are well correlated, proving that the nature of high-cycle fatigue is captured relatively well with the multiaxial criteria in the frequency domain. Furthermore, it stands as a proof that the complete procedure, from the stress-response calculation to the frequency-domain cycle-count estimate, is feasible and gives useful estimates for vibrating structures experiencing a notable dynamic

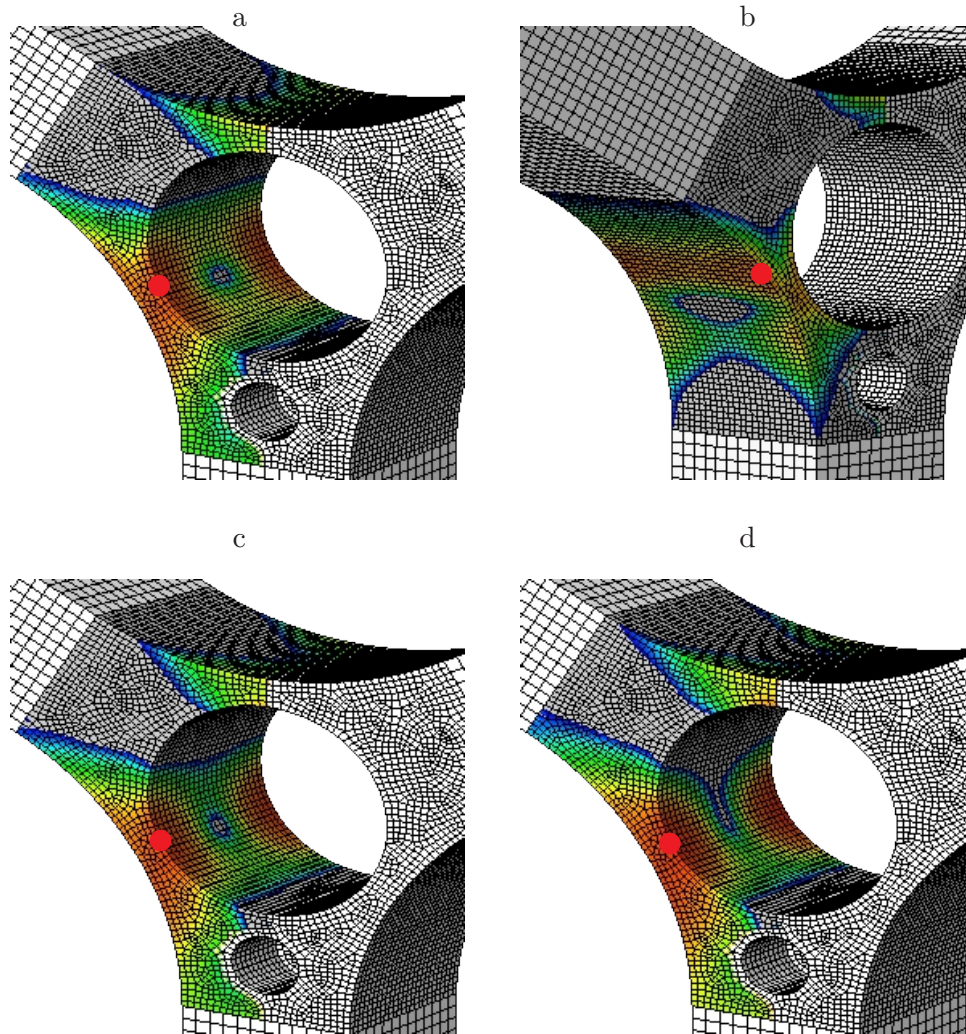


Figure 14: Position of critical points for load cases 2 (a), 3 (b), 6 (c) and 8 (d) as calculated with the C-S multiaxial criterion. The red dot indicates the location of the crack.

response.

## References

- [1] Ed Habtour, William Skip Connon, Michael F Pohland, Samuel C Stanton, Mark Paulus, and Abhijit Dasgupta. Review of response and damage of linear and nonlinear systems under multiaxial vibration. *Shock and Vibration*, 2014, 2014.
- [2] N. M. M. Maia and J. M. M. Silva. *Theoretical and Experimental Modal Analysis*. Research Studies Press, 1997.
- [3] Adam Niesłony and Ewald Macha. *Spectral Method in Multiaxial Fatigue*. Springer-Verlag Berlin Heidelberg, 2007.
- [4] Darrell F. Socie and Gary B. Marquis. *Multiaxial Fatigue*. Society of Automotive Engineers Inc, 1999.
- [5] I. Rychlik. Fatigue and stochastic loads. *Scand. J. Stat.*, 23(4):387–404, 1996.

- [6] A Halfpenny. A frequency domain approach for fatigue life estimation from finite element analysis. In M. D. Gilchrist, J. M. DulieuBarton, and K. Worden, editors, *DAMAS 99: Damage Assessment of Structures*, volume 167-1 of *Key Engineering Materials*, pages 401–410, 1999.
- [7] L. D. Lutes and S. Sarkani. *Random vibrations: analysis of structural and mechanical systems*. Elsevier, 2004.
- [8] M. Matsuishi and T. Endo. Fatigue of metals subject to varying stress. *Paper presented to Japan Society of Mechanical Engineers, Fukuoka, Japan*, 1968.
- [9] MA Miner. Cumulative damage in fatigue. *J. Appl. Mech.*, 12:A159–A164, 1945.
- [10] A. Palmgren. Die lebensdauer von kugellagern. *VDI-Zeitschrift*, 68:339–341, 1924.
- [11] D. Benasciutti and R. Tovo. Spectral methods for lifetime prediction under wide-band stationary random processes. *Int. J. Fatigue*, 27(8):867–877, August 2005.
- [12] Matjaž Mršnik, Janko Slavič, and Miha Boltežar. Frequency-domain methods for a vibration-fatigue-life estimation – application to real data. *International Journal of Fatigue*, 47:8–17, 2013.
- [13] W. N. Findley. A theory for the effect of mean stress on fatigue metals under combined torsion and axial load or bending. *Journal of Engineering for Industry*, pages 301–306, 1959.
- [14] K. Matake. An explanation on fatigue limit under combined stress. *Bulletin of the Japan Society of Mechanical Engineers*, 20:257, 1977.
- [15] D. L. McDiarmid. A shear stress based critical-plane criterion of multiaxial fatigue failure for design and life prediction. *Fatigue and fracture of engineering materials and structures*, 17(12):1475–1485, 1994.
- [16] A. Cristofori, L. Susmel, and R. Tovo. A stress invariant based criterion to estimate fatigue damage under multiaxial loading. *International Journal of Fatigue*, 30:1646–1658, 2008.
- [17] X. Pitoiset, A. Preumont, and A. Kernilis. Tools for a multiaxial fatigue analysis of structures submitted to random vibrations. ESA, 1999.
- [18] B. Li and M. Freitas. A procedure for fast evaluation of high-cycle fatigue under multiaxial random loading. *Journal of Mechanical Design*, 124:558–563, 2002.
- [19] A. Cristofori, D. Benasciutti, and Tovo R. A stress invariant based spectral method to estimate fatigue life under multiaxial random loading. *International Journal of Fatigue*, 33:887–899, 2011.
- [20] Ioannis V. Papadopoulos, Piermaria Davoli, Carlo Gorla, Mauro Filippini, and Andrea Bernasconi. A comparative study of multiaxial high-cycle fatigue criteria for metals. *Int. J. Fatigue*, 19(3):219–235, 1997.
- [21] B.-R. You and S.-B. Lee. A critical review on multiaxial fatigue assessment of metals. *International Journal of Fatigue*, 18:235–244, 1996.
- [22] Krzysztof Kluger. Fatigue life estimation for 2017a-t4 and 6082-t6 aluminium alloys subjected to bending-torsion with mean stress. *International Journal of Fatigue*, 80:22–29, 2015.
- [23] C Han, X Chen, and KS Kim. Evaluation of multiaxial fatigue criteria under irregular loading. *International Journal of Fatigue*, 24(9):913–922, 2002.
- [24] DF Socie, SD Downing, and S Utagawa. Benchmark problems in multiaxial fatigue. In *ICMFF10*, 2015.

- [25] Aleksander Karolczuk and Ewald Macha. A review of critical plane orientations in multiaxial fatigue failure criteria of metallic materials. *International Journal of Fracture*, 134:267–304, 2005.
- [26] Yi Sun Jingran Ge and Zhou Song. Fatigue life estimation under multiaxial random loading by means of the equivalent lemaître stress and multiaxial s-n curve methods. *International Journal of Fatigue*, 79:65–74, 2015.
- [27] Adam Niesłony. Comparison of some selected multiaxial fatigue failure criteria dedicated for spectral method. *Journal of Theoretical and Applied Mechanics*, 48:233–254, 2010.
- [28] X. Pitoiset and A. Preumont. Spectral methods for multiaxial random fatigue analysis of metallic structures. *International Journal of Fatigue*, 22:541–550, 2000.
- [29] Murat Aykan and Mehmet Çelik. Vibration fatigue analysis and multi-axial effect in testing of aerospace structures. *Mechanical Systems and Signal Processing*, 23(3):897–907, 2009.
- [30] Chan-Jung Kim, Yeon June Kang, and Bong-Hyun Lee. Experimental spectral damage prediction of a linear elastic system using acceleration response. *Mechanical Systems and Signal Processing*, 25(7):2538–2548, 2011.
- [31] J Ge, Y Sun, S Zhou, L Zhang, Y Zhang, and Q Zhang. A hybrid frequency–time domain method for predicting multiaxial fatigue life of 7075-t6 aluminium alloy under random loading. *Fatigue & Fracture of Engineering Materials & Structures*, 2014.
- [32] Martin Česnik, Janko Slavič, and Miha Boltežar. Uninterrupted and accelerated vibrational fatigue testing with simultaneous monitoring of the natural frequency and damping. *Journal of Sound and Vibration*, 331(24):5370–5382, 2012.
- [33] Mark Edward Paulus. *Fatigue damage accumulation due to complex random vibration environments: application to single-axis and multi-axis vibration*. PhD thesis, University of Maryland, College Park, 2011.
- [34] Andrea Carpinteri, Andrea Spagnoli, and Sabrina Vantadori. Reformulation in the frequency domain of a critical plane-based multiaxial fatigue criterion. *International Journal of Fatigue*, 67:55–61, 2014.
- [35] A. Preumont and V. Piéfort. Predicting random high cycle fatigue life with finite elements. *Journal of Vibration and Acoustics*, 116:245–248, 1994.
- [36] Julius S. Bendat and Allan G. Piersol. *Random Data: Analysis and Measurement Procedures*. Wiley, 2010.
- [37] D. E. Newland. *An introduction to Random vibrations and spectral analysis*. Longman Scientific & Technical, 1993.
- [38] J. W. Miles. On structural fatigue under random loading. *J. Aeronaut. Soc.*, 21:753–762, 1965.
- [39] T. Dirlik. *Application of Computers in Fatigue Analysis*. PhD thesis, The University of Warwick, 1985.
- [40] Martin Česnik, Janko Slavič, Primož Čermelj, and Miha Boltežar. Frequency-based structural modification for the case of base excitation. *Journal of Sound and Vibration*, 332(20):5029–5039, 2013.
- [41] Tadej Kranjc, Janko Slavič, and Miha Boltežar. A comparison of the strain and the classic experimental modal analysis. *Journal of Vibration and Control*, 2014.

- [42] X. Pitoiset, Rychlik I., and Preumont A. Spectral methods to estimate local multiaxial fatigue failure for structures undergoing random vibrations. *Fatigue & Fracture of Engineering Materials & Structures*, 24:715–727, 2001.
- [43] Denis Benasciutti. Some analytical expressions to measure the accuracy of the "equivalent von mises stress" in vibration multiaxial fatigue. *Journal of Sound and Vibration*, 333:4326–4340, 2014.
- [44] M. H. A. Bonte, A. de Boer, and R. Liebrechts. Determining the von mises stress power spectral density for frequency domain fatigue analysis including out-of-phase stress components. *Journal of Sound and Vibration*, 302:379–386, 2007.
- [45] Andrea Carpinteri and Andrea Spagnoli. Multiaxial high-cycle fatigue criterion for hard metals. *International Journal of Fatigue*, 23(2):135–145, 2001.
- [46] Martin Česnik and Janko Slavič. Vibrational fatigue and structural dynamics for harmonic and random loads. *Journal of Mechanical Engineering*, 60:339–348, 2014.
- [47] Jeong-Tae Kim, Yeon-Sun Ryu, Hyun-Man Cho, and Norris Stubbs. Damage identification in beam-type structures: frequency-based method vs mode-shape-based method. *Engineering structures*, 25:57–67, 2003.
- [48] C. Zhu, R. H. Byrd, and J. Nocedal. L-bfgs-b: Algorithm 778: L-bfgs-b, fortran routines for large scale bound constrained optimization. *ACM Transactions on Mathematical Software*, 23(4):550–560, 1997.
- [49] M. Kurek and T. Łagoda. Comparison of the fatigue characteristics for some selected structural materials under bending and torsion. *Journal of Materials Science*, 47:59–67, 2011.